Microstructure and shear rheology of entangled wormlike micelles in solution

Matthew W. Liberatore[a)]

Department of Chemical Engineering, Colorado School of Mines, Golden, Colorado 80401

Florian Nettesheim

DuPont Central Research and Development, Wilmington, Delaware 19880

Paula A. Vasquez, Matthew E. Helgeson, Norman J. Wagner, and Eric W. Kaler

Department of Chemical Engineering, University of Delaware, Newark, Delaware 19716

L. Pamela Cook

Department of Mathematics, University of Delaware, Newark, Delaware 19716

Lionel Porcar

National Institute of Standards and Technology, NIST Center for Neutron Research, University of Maryland, Gaithersburg, Maryland 20878

Y. Thomas Hu

Unilever Research and Development, Trumbull, Connecticut 06611

(Received 30 July 2008; final revision received 21 December 2008)

Synopsis

The shear rheology of a model wormlike micellar solution exhibits moderate shear thinning and curved flow velocity profiles without discontinuity (nonbanding case). The shear rheology and the flow kinematics are analyzed within the framework of the Giesekus constitutive equation. Macroscopically, the steady state flow curve of the solution exhibits shear thinning with a shear exponent <1 without hysteresis, indicative of a sample that does not shear band. The microstructure of the micellar network is probed by the combination of dynamic rheology, rheo-optics, and SANS. Flow kinematics in a Couette geometry are measured by particle tracking velocimetry and found to be consistent with predictions of the Giesekus constitutive equation fit to

[a)]Electronic mail: mliberat@mines.edu

the bulk shear rheology. 1-2 plane SANS measurements of the segmental alignment under shear are also found to be in agreement with predictions of the constitutive equation, providing a coherent picture of the mechanisms by which wormlike micelles flow and shear thin. The degree of segmental alignment is found to lag behind predictions of the model, which is postulated to be a consequence of the long, branched topology of the wormlike micelles. © *2009 The Society of Rheology.* [DOI: 10.1122/1.3072077]

I. INTRODUCTION

Wormlike micellar (WLM) solutions have been studied extensively as model viscoelastic fluids for more than two decades. Their remarkable rheologically simple behavior originates from their equilibrium structure, which leads to an apparent single relaxation process [Cates (1990, 1996, 1987)]. The viscoelastic properties depend on the solution conditions, i.e., surfactant solubility, concentration, type, and concentration of counter ions (in ionic surfactants). These parameters control microstructural features such as micellar contour length, mesh size, entanglement, and persistence length as well as scission and recombination kinetics [Berret (2005); Candau *et al.* (1989); Cates (1990, 1996, 1987); Couillet *et al.* (2004); Croce *et al.* (2003); Raghavan and Kaler (2001); Raghavan *et al.* (2002); Schubert *et al.* (2004b)].

Theoretical complexity arises close to a phase transition, where many WLM solutions exhibit shear banding. This phenomenon has been studied experimentally and it has been suggested that for some system it is linked to a shear-induced disorder-order transition to a nematiclike state [Berret (2005); Britton and Callaghan (1997); Cappelaere *et al.* (1997); Caputo *et al.* (2002); Croce *et al.* (2003); Decruppe *et al.* (2001); Hu and Lips (2005); Hu *et al.* (1998, 2008); Porte *et al.* (1997); Salmon *et al.* (2003)]. Other systems, such as the cationic surfactant studied here, exhibit a shear induced phase separation upon shear banding [Liberatore *et al.* (2006); Schubert *et al.* (2004b)]. Theoretical studies link this phenomenon to an underlying instability in the stress constitutive relation [Fielding and Olmsted (2003, 2004); Olmsted (1999); Porte *et al.* (1997)]. However, the structural cause for shear banding is still an active subject of research.

A number of models for viscoelastic fluids are based on the upper convected Maxwell model. Recently, the Giesekus model has been shown to capture the linear viscoelasticity as well as the nonlinear viscoelasticity of WLM solutions [Yesilata *et al.* (2006)]. The Giesekus model includes an anisotropic segmental mobility parameter α, which interestingly allows the distinction between shear banding and nonbanding flow. For values of $\alpha < 0.5$ the stress-rate constitutive relation is monotonically increasing and the fluid does not shear band. If $\alpha > 0.5$, the constitutive relation is non-monotonic, which leads to shear banding. Details of the Giesekus model will be discussed in the theory section.

Yesilata *et al.* (2006) studied the linear, nonlinear shear, and extensional rheology of erucyl bis(hydroxyethyl)methylammonium chloride (EHAC)/ ammonium chloride (NH_4Cl) solutions to test the Giesekus model. They demonstrate that the Giesekus model not only successfully describes the steady state stress, but also the hysteresis observed in an up/down step rate experiment for shear banding fluids. The mobility parameter α captures the severity of this hysteresis as a function of salt concentration or temperature and sheds light on the extent that the sample shear bands.

In this contribution we take the comparison further to closely examine the connection between *microstructure*, linear and nonlinear viscoelasticity, and flow kinematics for a nonbanding sample. A unique gap-resolved 1-2 plane SANS flow cell [Liberatore *et al.* (2006)] provides the first direct measurement of the local microstructure. When combined with PTV measurements of the flow kinematics, the macroscopic stress (measured or predicted) can be connected with the segmental orientation tensor measured by flow-

SANS. In doing so, a methodology to connect flow kinematics and microstructure is established.

II. THEORY

A. The Giesekus constitutive model

The governing equations for the fluid flow are as follows. Conservation of mass for an incompressible fluid is

$$\nabla \cdot \mathbf{v} = 0. \tag{1}$$

Conservation of momentum for inertialess flow is

$$\nabla \cdot \mathbf{\Pi} = 0, \tag{2}$$

where

$$\mathbf{\Pi} = p\mathbf{I} - \eta_\infty \dot{\boldsymbol{\gamma}} + \boldsymbol{\tau}_p \tag{3}$$

is the total stress. Here the shear rate is $\dot{\boldsymbol{\gamma}} = \nabla\mathbf{v} + (\nabla\mathbf{v})^{\mathsf{T}}$, p is the pressure, η_∞ is the infinite shear viscosity, and $\boldsymbol{\tau}_p$ is the extra stress.

In this work, the extra stress in the nonlinear constitutive equation proposed by Giesekus is used [Giesekus (1982a, 1982b)]. This model can be derived from dumbbell theory assuming a non-isotropic drag coefficient or mobility, i.e., the reciprocal of the drag coefficient, of the beads on the dumbbells. For steady shear flow, the Giesekus model predicts shear thinning and nonvanishing first and second normal stress differences. The nonvanishing second normal stress difference is a direct result of the anisotropic drag [Giesekus (1982b)]. This model has been used to describe shear and elongational flow of another system of wormlike micelles in Yesilata *et al.* (2006).

In tensorial form, the Giesekus model [Giesekus (1982a, 1982b)] for a single relaxation mode is

$$\left(\mathbf{I} + \frac{\alpha}{G_0}\boldsymbol{\tau}_p\right) \cdot \boldsymbol{\tau}_p + \lambda_r \boldsymbol{\tau}_{p(1)} = \lambda_r G_0 \dot{\boldsymbol{\gamma}}. \tag{4}$$

Here $(\cdot)_{(1)}$ denotes the upper convected derivative. The model has four parameters to fit to experimental data: η_∞, the plateau modulus, G_0; the relaxation time, λ_r; and the dimensionless "mobility factor" α. In the linear viscoelastic regime, the Giesekus model reduces to a single Maxwell mode, i.e.,

$$\tau_{r\theta} = G_0\left\{\frac{(\lambda_r\omega)^2}{1+(\lambda_r\omega)^2} + i\left(\frac{\lambda_r\omega}{1+(\lambda_r\omega)^2} + \eta_\infty\omega\right)\right\}. \tag{5}$$

Here, the shear stress $\tau_{r\theta}$ is written appropriately for a Couette geometry in cylindrical coordinates. Through fitting to linear viscoelastic experimental data the parameters λ_r (relaxation time) and G_0 (plateau modulus) can be obtained. The other parameters, α and η_∞, are found through fitting to the experimental data of the viscosity in steady shear flow. As the model parameters can be defined solely from the shear viscosity and linear viscoelasticity, other rheological functions (such as the first and second normal stress differences) and microstructural parameters (such as the segmental order parameter and degree of segmental flow alignment) are predictions of the model.

In simple, steady state Couette flow $\mathbf{v} = (0, v(r), 0)$ and Eq. (4) gives

$$\tau_{rr} + \frac{\alpha}{G_0}(\tau_{rr}^2 + \tau_{r\theta}^2) = 0, \tag{6a}$$

$$\tau_{r\theta} - \lambda_r \dot{\gamma}_0 \tau_{rr} + \frac{\alpha}{G_0}(\tau_{\theta\theta} + \tau_{rr})\tau_{r\theta} = \lambda_r G_0 \dot{\gamma}_0, \tag{6b}$$

$$\tau_{\theta\theta} - 2\lambda_r \dot{\gamma}_0 \tau_{r\theta} + \frac{\alpha}{G_0}(\tau_{\theta\theta}^2 + \tau_{r\theta}^2) = 0, \tag{6c}$$

$$\tau_{zz} + \frac{\alpha}{G_0}\tau_{zz}^2 = 0. \tag{6d}$$

Equations (6) are then coupled with the equation of motion (2) through

$$\frac{1}{r}\frac{\partial}{\partial r}[r^2(\tau_{r\theta} - \eta_\infty \dot{\gamma}_0)] = 0, \tag{7}$$

where the shear rate is

$$\dot{\gamma}_0 = \frac{\partial v}{\partial r} - \frac{v}{r}. \tag{8}$$

To solve the model under steady state Couette flow, Eqs. (6) are solved numerically for the shear stress as a function of the applied nominal shear rate. This relationship is used to integrate Eq. (7) using no-slip boundary conditions for the velocity:

$$v(r = r_i) = v_i, \tag{9}$$

$$v(r = r_o) = 0, \tag{10}$$

where r_i and r_o are the inner and outer radius, respectively, d is the gap size, and v_i is the inner wall velocity applied by the rheometer. Now, the velocity profiles across the gap for different nominal shear rates are obtained, and the local shear rates are found from Eq. (8). Next, predictions from the model for the stress components as functions of the local shear rate are then used to find the alignment factor and orientation angle as follows.

The orientation angle β, for the Giesekus model [Giesekus (1982a)], is given by

$$\zeta^2 = \frac{C_I}{C_{II}} = \cot^2 \beta, \tag{11}$$

where C_I and C_{II} are, respectively, the first and second invariants of the configuration tensor $\mathbf{C}$ defined as

$$\mathbf{C} = \frac{\boldsymbol{\tau}_p}{G_0} + \mathbf{I}. \tag{12}$$

Then, from Eq. (6) assuming steady state, ζ can be found as [Giesekus (1982a)]

$$\zeta = \frac{1}{2}\frac{N_1}{\tau_{r\theta}} + \frac{1}{2}\sqrt{\left(\frac{N_1}{\tau_{r\theta}}\right)^2 + 4}, \tag{13}$$

where $N_1 = \tau_{\theta\theta} - \tau_{rr}$ is the first normal stress difference.

Additionally, the order tensor $\mathbf{S}$ describing the difference in average conformation of the chains from equilibrium (isotropic) is given by [Giesekus (1982a)]

$$\mathbf{S} = \frac{\mathbf{C}}{\mathrm{tr}(\mathbf{C})} - \frac{1}{3}\mathbf{I}. \tag{14}$$

Similarly, the alignment factor in the 1-2 plane can be defined as the sum of the largest eigenvalues of the order tensor as follows:

$$A_f = 3(S_{11} + S_{22}) = \frac{\tau_{11} + \tau_{22}}{3G_0 + \tau_{11} + \tau_{22}}. \tag{15}$$

III. EXPERIMENTAL

A. Solution preparation

The cationic surfactant system studied here has been described previously [Schubert *et al.* (2004b)] and so will only be summarized here. The surfactant is erucyl bis(hydroxyethyl)methylammonium chloride (EHAC), C_8H_{17}-CH═CH-$C_{12}H_{24}$-N($C_2H_4OH)_2CH_3Cl$ (Akzo Nobel) with sodium salicylate(o-hydroxy benzoate) (NaSal) (ACS-grade reagent, Sigma-Aldrich) in Nanopure deionized water (>18 MΩ-cm). The solution of interest is 40 mM EHAC and 1000 mM NaSal. Samples were prepared by mixing stock solutions of surfactant and salt with water. After vortex mixing for 30 s, the samples were left at rest for 1 day before use. Samples for SANS were prepared in D_2O (Cambridge Isotopes) to obtain maximum contrast in the neutron scattering. Of note, changing the solvent from DI water to D_2O causes only small differences in the rheology and phase behavior. All experiments were performed at 24 ± 1 °C unless otherwise noted.

B. Rheology and rheo-optics

Steady shear and dynamic rheological measurements were carried out on a AR-G2 rheometer (TA instruments, New Castle, DE) with a 40 mm, 2° cone. An ARES rheometer (TA Instruments, New Castle, DE) with optical analysis module was used to perform the rheo-optic experiments. A Couette cell with 15 mm inner radius, 2 mm gap, and 20 mm path length was used when measuring birefringence, dichroism, and transmission. A linearly polarized He–Ne laser (λ_0=632.8) projects down the vorticity direction for measurements in the flow-shear gradient plane.

C. Velocimetry

The details of the experimental setup for the particle tracking velocimetry experiments are available elsewhere [Hu and Lips (2005)]. In brief, the custom made Couette flow cell is driven by a commercial rheometer (MCR 500, Anton Paar). The outer, stationary cylinder is a quartz cooling jacket while the inner cylinder is anodized aluminum. The inner radius is 16 mm with a 1.5 mm gap. The samples are seeded with ~10 μm glass spheres (TSI Fluid) at 100 parts per million by weight, which does not alter the rheology. The laser sheet used to visualize the flow field is positioned to minimize the influence of end effects of the flow field on the data. The velocity profiles presented in this work are at steady state. For each run, the velocities of over 1500 tracer particles were recorded and separated into 100 bins across the gap and subsequently averaged with a one standard deviation error bar. The x-axis is the normalized gap for all velocity profiles presented in this work where 0 defines the inner, rotating wall and 1 is the outer, stationary cylinder.

D. Small-angle neutron scattering under flow

Rheo-SANS measurements were conducted on the NG7 30-m small-angle scattering instrument at the Center for Neutron Research at the National Institute of Standards and Technology (NIST) in Gaithersburg, MD. Scattering images were taken at a wavelength of 6 Å and detector distances of 4 and 15 m yielding a q-range of 0.003 to 0.13 $Å^{-1}$,

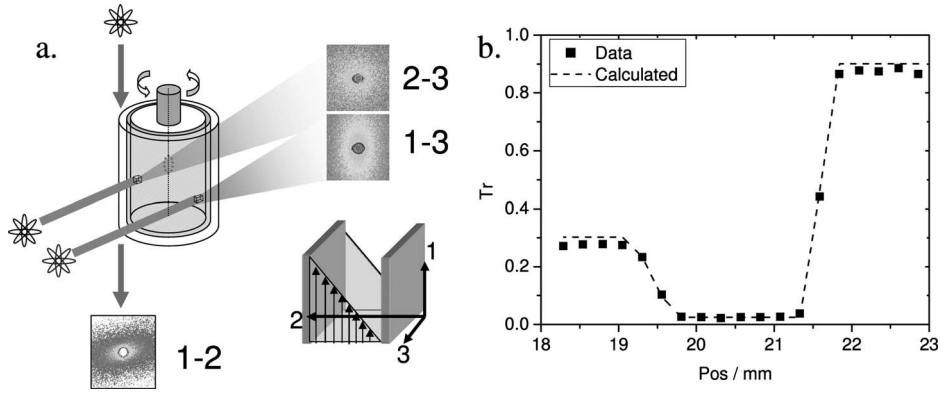

FIG. 1. (a) Schematic of SANS in all three projection of a shear cell. (b) Transmitted counts versus gap position for the custom made 1-2 plane shear cell.

which probes the cross section and persistence length of the micelles, such that segmental orientation is measured. Data were corrected and normalized using standard techniques [Kline (2006)].

Measurements in the flow-vorticity (1-3) and shear gradient-vorticity (2-3) planes employed a Couette cell with aluminum cup and quartz bob (48 mm bob diameter, 1 mm gap, 70 mm height) controlled by a UDS 200 rheometer (Anton Parr, Ashland, VA) thermostatted to 24 °C ± 0.2 °C. The shear viscosity recorded during SANS experiments is within experimental error of previously reported values [Raghavan *et al.* (2002); Schubert *et al.* (2004b)].

Scattering patterns collected in the flow-shear gradient (1-2) plane used a custom made short-gap aluminum Couette cell (25 mm inner radius, 1.35 mm gap, and 5 mm path length) (Fig. 1) [Liberatore *et al.* (2006)]. A slit preceding the cell reduced the neutron beam to 0.3 mm in width by 5.0 mm in height. The gap was defined by transmission measurements [Fig. 1(b)]. Theoretical calculations accounting for the scattering density of aluminum (cell) and the blank sample (D_2O/H_2O mixture) were used to help align the slit. Reduced beam positions of 0.2, 0.5, 0.8, and 1.2 mm from the inner (rotating) wall were selected for subsequent scattering measurements. A slight reflection (most likely due to the wall) was observed at the 1.2 mm gap position (outer). When the reflection was seen, azimuthal averages (used to find alignment factor and orientation angle) used data from only 90° (flow direction) to 270°. A stepper motor was used to rotate the inner cylinder resulting in shear rates from 0.1 to 100 s^{-1}. Positive shear rates correspond to a counter-clockwise rotation of the inner cylinder with respect to the incident neutrons. Experiments were performed at $\lambda = 6$ Å, $\Delta\lambda = 22\%$ to optimize the flux of neutrons. A circulating water bath provided temperature control for the custom Couette cell (24 °C ± 0.5 °C).

To quantify the scattering, an alignment factor [Walker and Wagner (1996)] is calculated from the 2-D scattering patterns as

$$A_f(q) = \frac{\int_0^{2\pi} I(q,\phi)\cos(2\phi - \beta)d\phi}{\int_0^{2\pi} I(q,\phi)d\phi}. \tag{16}$$

The angle ϕ is defined from the flow direction for the 1-3 and 1-2 scattering, and from the gradient direction for 2-3 scattering. The angle β accounts for the orientation of the principal axis of the scattering with respect to the flow direction ($\beta = 0$ along the

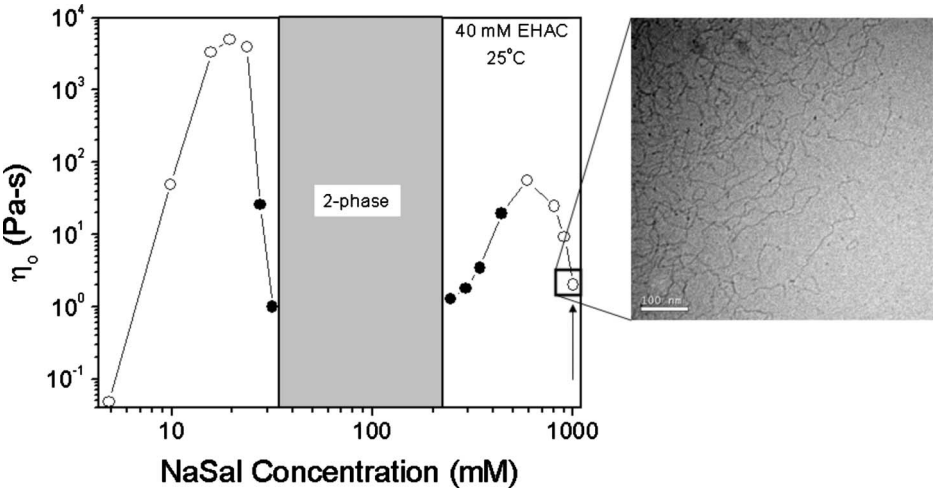

FIG. 2. Zero shear viscosity at 25 °C for 40 mM EHAC at various NaSal concentrations [Raghavan *et al.* (2002)]. Filled symbols indicate sample exhibiting SIPS. The arrow indicates the sample investigated in this work. A cryo-TEM image for this sample is shown to the right.

1-direction). Complete alignment with the flow corresponds to an alignment factor of $A_f=-1$ while $A_f=0$ indicates an isotropic segmental alignment. The alignment factors and orientation angles are reported for $q=0.03$ Å^{-1}, which is within the region where the alignment factor is independent of q and corresponds to length scales smaller than the characteristic mesh or entanglement lengths.

IV. RESULTS

A. Phase behavior

The phase behavior of this system was reported previously [Raghavan *et al.* (2002); Schubert *et al.* (2004b)]. The viscosity "phase diagram" at fixed EHAC concentration (40 mM) and temperature (25 °C) (Fig. 2) shows two viscosity maxima bordering a two phase region. At low salt concentrations the viscosity builds as the wormlike micelles grow in length. A maximum in the viscosity is observed at approximately 20 mM NaSal [Schubert *et al.* (2004a)] followed by a steep decrease in the viscosity before thermodynamic phase separation occurs at intermediate salt concentrations. The two-phase region consists of a dense network phase and a brinelike phase. At higher salt concentrations, another single phase region is observed and the viscosity displays a second, weaker maximum with increased salt concentration. Compositions marked with solid, black circles in Fig. 2 exhibit shear-induced phase separation. The sample examined here, 40 mM EHAC 1000 mM NaSal, is selected to be well beyond the two-phase region and second viscosity maximum. Cryo-TEM reveals a threadlike microstructure (Fig. 2) with the presence of both junctions and overlapping micelles, as expected [Nettesheim and Kaler (2007)].

B. Equilibrium microstructure by rheology, rheo-optics, and SANS

Rheology, rheo-optics, and scattering provide a detailed, quantitative measure of the microstructure in solutions of wormlike micelles at equilibrium, i.e., in the linear viscoelastic regime. The important length scales, i.e., contour length, L_c, entanglement

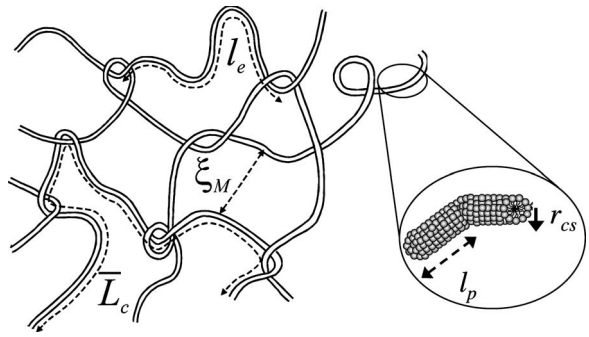

FIG. 3. Schematic of important length scales of an idealized wormlike micelle network [Schubert *et al.* (2003)].

length, l_e, mesh size, ξ_M, persistence length, l_p, and cross-sectional radius, r_{CS} are experimentally accessible through dynamic rheology, birefringence, and small-angle neutron scattering (SANS) measurements (see Fig. 3) [Schubert *et al.* (2003)]. Table I summarizes the length and time scales for the entangled wormlike micellar solution.

The dynamic rheological response of the sample (Fig. 4) illustrates linear viscoelasticity typical of entangled wormlike micelles. In general, the storage (G') and loss (G'') moduli demonstrate Maxwellian behavior (i.e., single relaxation time) at low and intermediate frequencies. A liquidlike response ($G'' > G'$) at low frequencies becomes rubbery at higher frequencies.

As noted earlier, the Giesekus model reduces to the Maxwell model in the limit of small strain amplitudes (solid and dashed lines in Fig. 4). The terminal relaxation time, λ_r, and the plateau modulus, G_0, are determined by fitting the data to Eq. (5) using the value of η_∞ fit from steady shear rheology discussed later. The breakage time (λ_{br}) of the wormlike micelles is found from the inverse of the frequency at $G''_{\min}$. The reptation time (λ_{rep}) is calculated as $\lambda_{rep} = \lambda_r^2/\lambda_{br}$ [Cates (1987); Granek and Cates (1992)]. The agreement between the data and Maxwell model (Fig. 4) shows that reptation time and breakage time are separated enough to treat these solutions as being in the fast breaking limit.

Using the minimum in the loss modulus and plateau value of the storage modulus in cooperation with the stress optic coefficient from rheo-optic experiments, four of the five equilibrium length scales are determined and summarized in Table I [Cates (1990); de Gennes (1979); Doi and Edwards (1986); Granek and Cates (1992); Kuhn and Grun (1942); Schubert *et al.* (2003); Shikata *et al.* (1994)].

The 40 mM EHAC 1000 mM NaSal sample remains clear with negligible turbidity and dichroism for all shear rates investigated [Fig. 5(a)]. Therefore, no shear induced

TABLE I. Summary of length scales and time scales.

Property	Value
ξ_M (nm)	55 ± 1.7
l_p (nm)	10.3 ± 0.2
l_e (nm)	170 ± 11
L_c (nm)	940 ± 70
r_{CS} (nm)	2.3 ± 0.2
λ_{br} (s)	0.013 ± 0.001
λ_{rep} (s)	10.0 ± 0.4

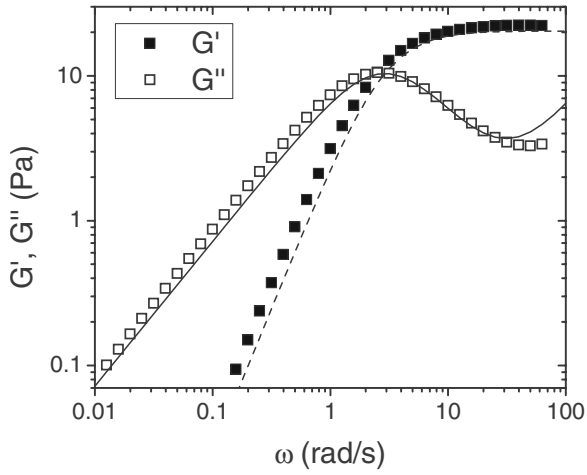

FIG. 4. Storage (G′) and loss (G″) moduli as a function of angular frequency for 40 mM EHAC 1000 mM NaSal. The dashed and solid lines represent the Giesekus fit to G′ and G″, respectively.

phase separation or concentration fluctuations are observed in the range of shear rates investigated here. In addition, the flow-birefringence provides insight into the segmental alignment of the polymeric molecules [Fig. 5(b)]. The solution shows a monotonically increasing birefringence at all rates measured. Therefore, the local segmental alignment continuously increases in the absence of phase change, as expected. The solution also observes the stress-optic rule at low shear rates/stress [Fig. 5(b), inset] which helped determine the persistence length. Also, the birefringence and its associated orientation angle are used to quantify the stress-optic coefficient and the first normal stress difference at low shear rates [Humbert and Decruppe (1998)].

The final length scale of interest, the average cross-sectional radius, is determined from small-angle neutron scattering. A fit of the form factor of a cylinder at high scattering vectors yields the average cross-sectional radius (Fig. 6). The deviation at low q, however, is due to excluded volume interactions between the charged micelles.

C. Shear rheology

The shear rheology of the 40 mM EHAC 1000 mM NaSal exhibits shear thinning, which is characteristic of entangled wormlike micelles in solution (Fig. 7). A zero shear plateau at low shear rates is followed by a shear thinning regime above a shear rate of $\sim 1\ s^{-1}$. The limiting slope in the shear thinning region is −0.80. Correspondingly, the stress [Fig. 7(b)] increases at all shear rates, although only gradually in the shear thinning regime. The first normal stress difference [Fig. 7(c)] scales with shear rate to the first power above $\sim 1\ s^{-1}$. The normal stresses are too low to be measured in the zero shear plateau, hence rheo-optical data complete the first normal stress data set [Humbert and Decruppe (1998)]. The lines in Fig. 7 are fits of the Giesekus model to the data (Table II). In the present case, the dynamic data provide λ_r and G_0. The zero shear rate viscosity for a Maxwell fluid follows from $G_0\lambda_r$. Parameters α and η_∞, the high shear viscosity ($\eta_{r,\infty} = \eta_\infty / \eta_0$), are determined by fitting the stress or conversely the viscosity curve to the Giesekus model. Note, the line in Fig. 7(c) is a prediction of the first normal stress difference, as all parameters are determined.

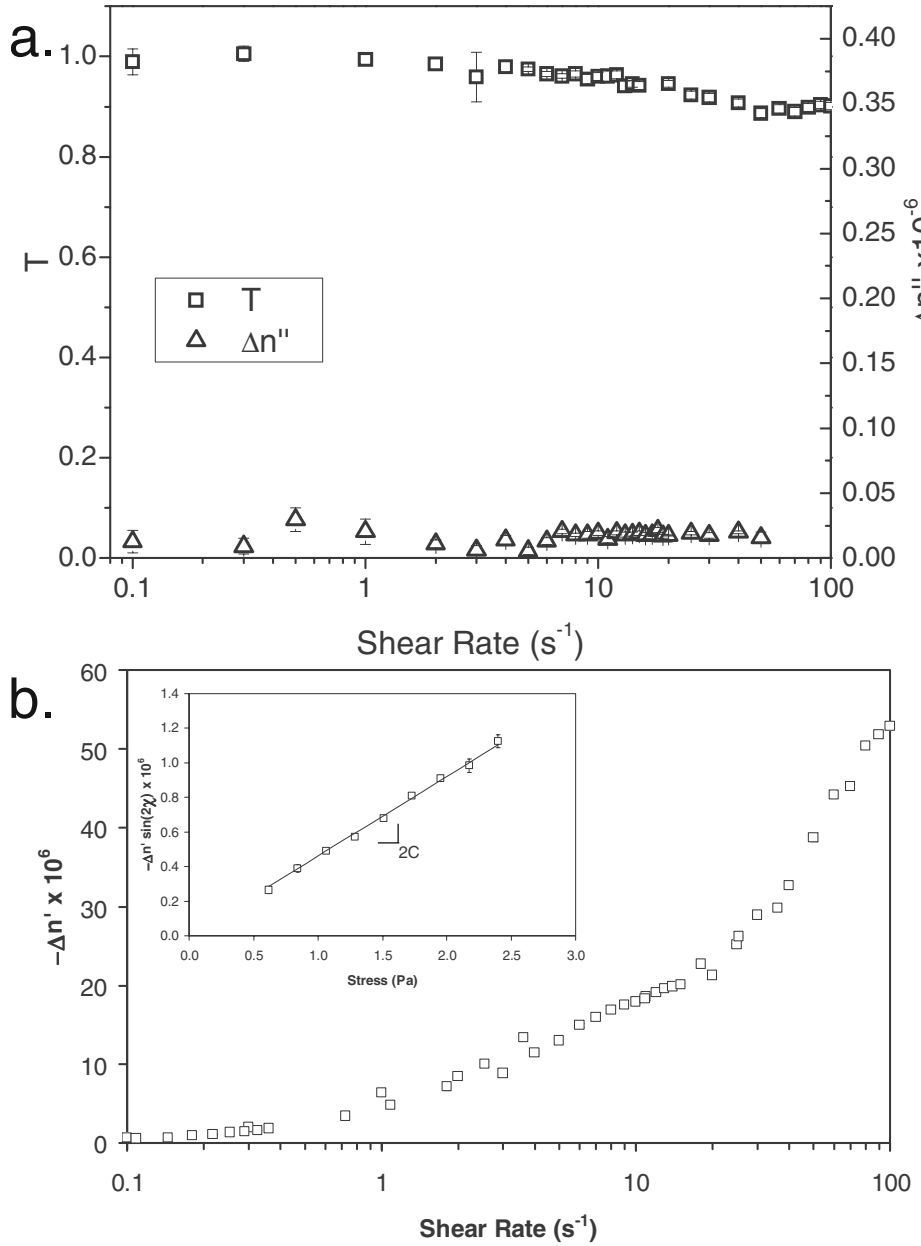

FIG. 5. (a) Transmittance and dichroism as a function of shear rate. (b) Steady state birefringence versus shear rate for 40 mM EHAC 1000 mM NaSal. (b) Inset: Determination of stress-optic coefficient, C, from birefringence data at low stress.

D. Velocity profiles

Velocity profiles for the 40 mM EHAC 1000 mM NaSal sample (Fig. 8) evolve essentially as expected for a power-law fluid. For shear rates in the zero shear plateau the velocity profile is nearly linear. As the sample begins to shear thin, curved velocity profiles are observed for shear rates between 10 and 100 s^{-1}. The deviation from a

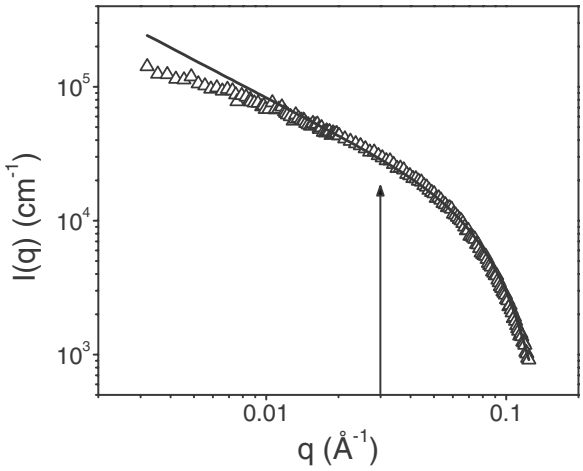

FIG. 6. Equilibrium, circularly averaged scattering intensity of 40 mM EHAC 1000 mM NaSal obtained in the rheo-SANS cell in the 1-3 plane of flow. The line fits a cylindrical form factor to the high-q part of the scattered intensity. The arrow indicates the q value at which subsequent annular averages were performed.

Newtonian shear profile increases for shear rates up to 20 s^{-1} before decreasing at higher shear rates. The Giesekus model, using the parameters obtained by fitting the dynamic and flow rheology (see Figs. 4 and 7), predicts the velocity profiles measured by PTV.

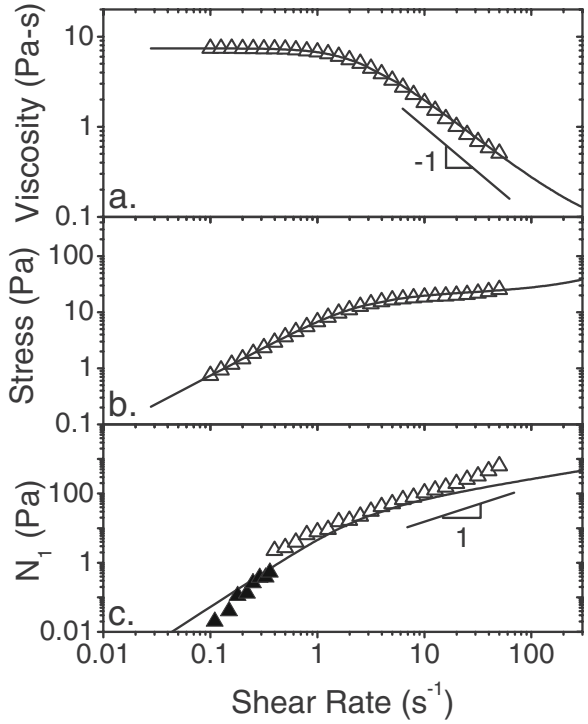

FIG. 7. Viscosity (a), stress (b), and first normal stress difference (c) as a function of shear rate for 40 mM EHAC 1000 mM NaSal. Lines represent the Giesekus fit to the data. Filled symbols are taken from rheo-optic data.

TABLE II. Summary of Giesekus fit parameters.

Parameter	Value
λ_r (s)	0.36
G_0 (Pa)	20.42
η_0 (Pa s)	7.35
α	0.45
$\eta_{r,\infty}$	0.002
η_∞ / η_0	0.007

E. Small-angle neutron scattering under flow

Rheo-SANS was performed in the 1-3 (radial beam) and 2-3 (tangential beam) planes. Flow-SANS measurements in the 1-2 plane included shear rates in the zero shear plateau to well into the shear thinning regime. Flow alignment of the wormlike micelles is qualitatively seen in 2-D scattering patterns in the 1-3 plane [Fig. 9(a)] while isotropic patterns are observed in the 2-3 plane [Fig. 9(b)]. This observation is an artifact of the asymmetry of the scattering volume in the 2-3 plane [Nettesheim *et al.* (2004)]. Flow-alignment of wormlike micelles in the shear thinning region has been previously reported for the 1-3 plane of flow [Schubert *et al.* (2004b)]. While measurements in the 1-3 plane provide quantitative measures of the average flow alignment, resolution along the gradient direction requires a custom flow cell to probe the 1-2 plane of flow. Gap resolved

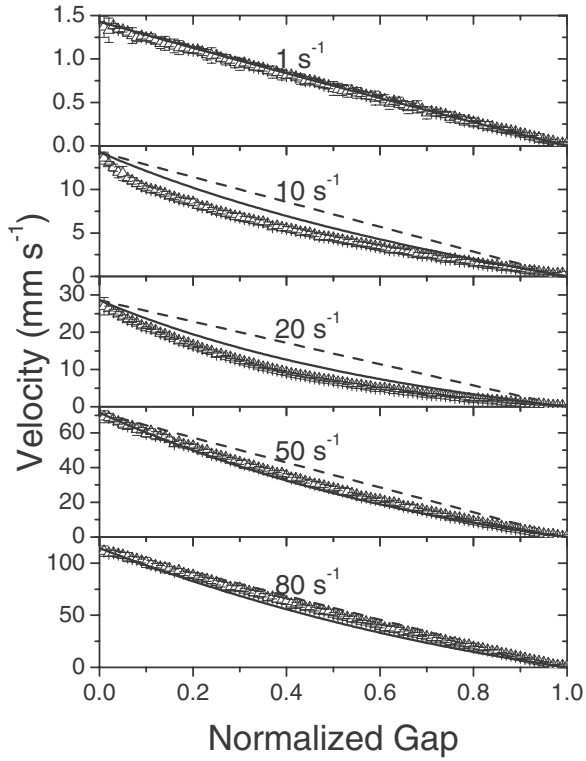

FIG. 8. Velocity profile versus normalized gap for 40 mM EHAC 1000 mM NaSal at five nominal shear rates.

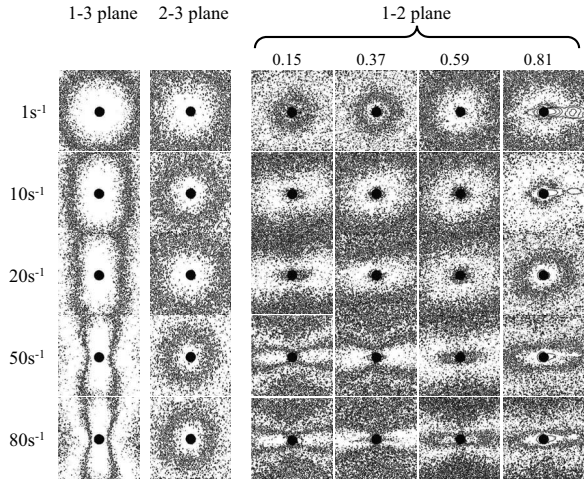

FIG. 9. Scattering patterns recorded at a detector setting of 15 m in the 1-3 plane (a), 2-3 plane (b), and 1-2 plane (c) of 40 mM EHAC 1000 mM NaSal at various shear rates. The normalized gap (0.15, 0.37, 0.59, 0.81) for the 1-2 plane is measured from the inner, rotating cylinder.

patterns in the 1-2 plane [Fig. 9(c)] offer insight into the local structure under flow. In general, the scattering at low shear rates is isotropic. Shear thinning is accompanied by anisotropy in the 1-3 and 1-2 planes. The anisotropy increases monotonically with shear rate (both 1-3 and 1-2 planes) and proximity to the rotating wall (at nominal gap of zero for the 1-2 plane). In addition, the orientation angle decreases, i.e., approaches the flow direction.

The segmental alignment of the wormlike micelles is quantified via the alignment factor in both 1-2 (gap resolved) and 1-3 (gap averaged) planes as a function of shear rate (Fig. 10). The magnitude of the alignment factors for 40 mM EHAC 1000 mM NaSal increase strongly in the shear thinning regime. Further, the gap resolved 1-2 plane results show a systematic increase in alignment with position moving toward the inner, rotating

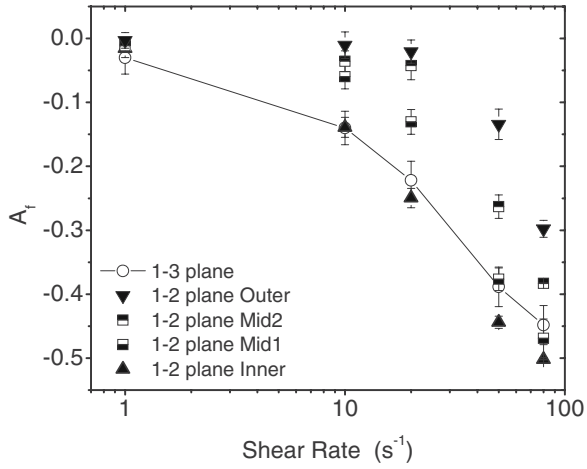

FIG. 10. Alignment factor in 1-3 and 1-2 planes as a function of nominal shear rate for 40 mM EHAC 1000 mM NaSal.

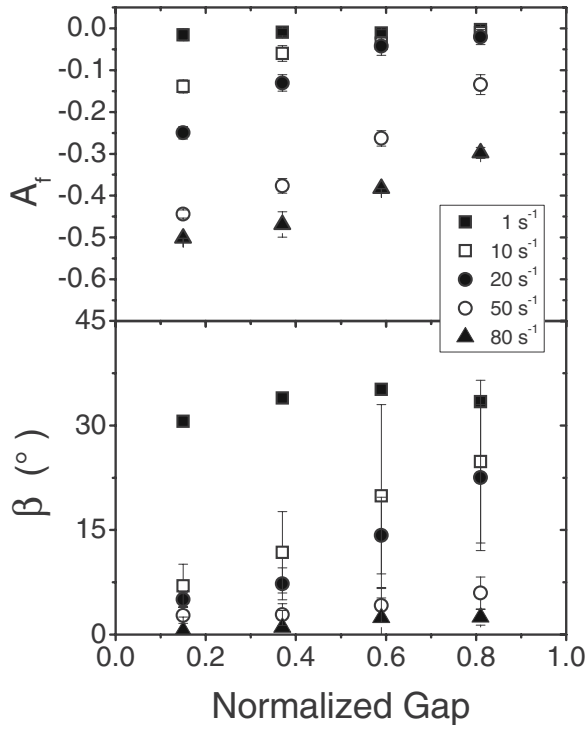

FIG. 11. Gap resolved alignment factor (top panel) and orientation angle (bottom panel) in the 1-2 plane for 40 mM EHAC 1000 mM NaSal as a function of the nominal shear rate.

cylinder. This result is expected as the shear rate increases systematically across the gap. The 1-3 plane measurements generally follow the 1-2 plane results. Note the 1-3 plane measurements are not simply an average over the corresponding 1-2 plane results as they correspond to different projections of the full, 3-D order tensor.

While previous SANS measurements in the 1-2 plane did not resolve different positions across the gap [Berret *et al.* (2000); Noirez (2000); Noirez and Lapp (1997)], our experiments measure the alignment and orientation angle as a function of gap position for four nominal shear rates (Fig. 11). Overall, the orientation angle decreases, while the magnitude of the alignment factor increases as the rotating, inner cylinder is approached. Orientation angles for the 40 mM EHAC 1000 mM NaSal sample approach full flow alignment (β=0).

V. DISCUSSION AND ANALYSIS

The Giesekus model successfully fits the linear viscoelastic and nonlinear shear viscosity data. The model then quantitatively predicts the measured first normal stress difference as well as the flow kinematics measured by PTV. Further, $\alpha \leq 0.5$, which agrees with absence of shear banding. We next test whether the segmental alignment factor and orientation angle follow the local velocity profile, as a variation in local shear rate across the gap of the Couette cell is observed. A quantitative test is made by computing the local shear rate from PTV measurements (Fig. 8) in a Couette cell and mapping the values onto the four gap positions measured in the 1-2 SANS cell. The dimensions of the two Couette cells are similar and therefore PTV measurements should translate from one cell to the

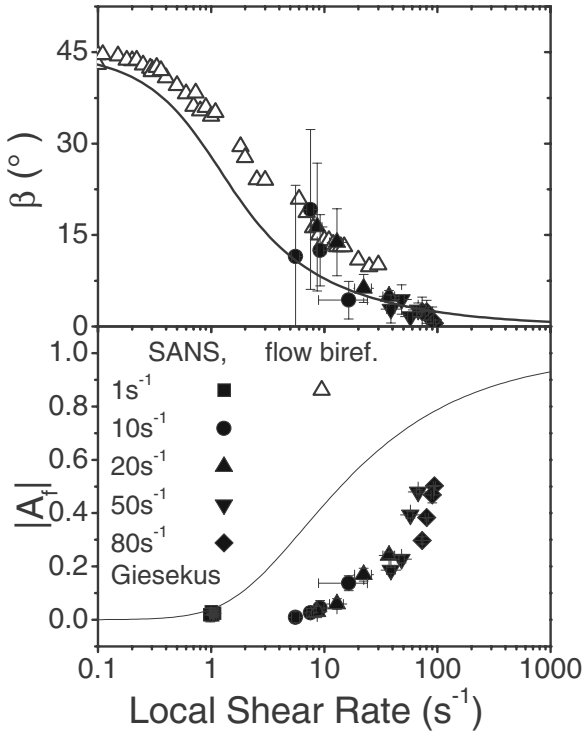

FIG. 12. Orientation angle (top) and alignment factor (bottom) as a function of local shear rate in the 1-2 plane for 40 mM EHAC 1000 mM NaSal. The lines are the Giesekus prediction for the orientation angle β and alignment factor from Eqs. (12) and (15).

other within experimental certainty. The shear rate is averaged over the width of the aperture used in the SANS experiment to yield the local shear rate corresponding to each gap-resolved SANS measurement. Thus, the alignment factor and orientation angle are replotted as a function of actual, local shear rate (Fig. 12).

As seen, the alignment factor and orientation angle transition continuously and smoothly from the expected values at low shear rates (A_f=0, β=45°) toward a flow-oriented state (β=0°) with moderate segmental alignment ($A_f \sim 0.5$). Flow birefringence data are used to augment the orientation angle as determination of weak alignment by SANS is difficult. This trend in the alignment factor and orientation angle is qualitatively expected for a solution of WLMs, which are often modeled as semi-flexible chains. Comparison to the shear rheology (Fig. 7) shows that significant shear thinning commences for shear rates around 1 s^{-1}. Also near 1 s^{-1}, significant flow alignment ($\beta \sim 15°$) is measured but the net segmental alignment is very small (A_f=0). Indeed, segmental alignment begins to be significant at much higher shear rates ($\sim$20 s^{-1}) while the measured average segmental orientation is nearly completely flow aligned. Thus the combination of 1-2 flow SANS, rheometry, and cryo-TEM demonstrate that the highly entangled and somewhat branched WLM solution responds in the nonlinear regime by stretching with the flow's extensional axis without substantial alignment at the segmental level. Only after substantial flow alignment of the WLM microstructure is significant segmental alignment observed. Note that the combination of 1-3, 2-3, and 1-2 plane

SANS measurements show that in-plane (1-2) alignment is dominant and that no propensity to align along the vorticity axis is observed (as is sometimes observed in fibrillar systems).

Turning to the Giesekus model predictions for the degree of segmental alignment, the model predicts earlier and stronger flow alignment than observed in experiment. This result is expected for this WLM system because the Giesekus model is cast in terms of the net end-to-end vector of the polymer chain, rather than the segmental alignment. For rigid rods or short, unbranched WLMs, the alignment should correspond well. However, this solution is comprised of very long, entangled micelles with evidence of three-junctions typical of micellar branching (Fig. 2). Then, it is not surprising that the SANS measurements of segmental alignment are not as large as the predictions from the Giesekus configurational tensor. The long micelles can have a net alignment while still having significant disorder at the segmental level. Furthermore, micelle branching would necessarily suppress alignment. Indeed, the fact that the model predictions show more flow orientation and significantly more alignment than the SANS measurements of the segmental orientation and net alignment is not unexpected for this microstructure. Measurements over a much longer length scale (lower "q" or momentum transfer) than currently accessible would be required for a more complete comparison. Nonetheless, good qualitative agreement between the model predictions and experimental observations is observed, and the quantitative disagreement is in the direction expected given the lack of complete correspondence between the physical properties being predicted by the model and those measured experimentally.

VI. CONCLUSION

A non-shear-banding wormlike micellar solution was studied using rheology, rheo-birefringence, particle tracking velocimetry, and flow SANS. The measurement of equilibrium structure and dynamics confirms the Maxwellian behavior of the WLM solution with a single relaxation time in the fast breaking limit. The flow curves of this solution display shear thinning but no stress plateau as well as a positive and increasing normal stress. Finally, using PTV, curved velocity profiles are observed in the shear thinning regime, while linear profiles are observed in the zero shear and the high shear limit. These observations are all consistent with a shear thinning viscoelastic fluid in the absence of shear banding.

The Giesekus model is uniquely suited for the description of WLM rheology and flow kinematics. Using dynamic and flow rheology to set the Giesekus model parameters, the velocity profile quantitatively agrees with the model predictions. In addition, microscopic information about the WLM solution is gained, namely the segmental alignment factor and orientation angle. Novel 1-2 plane flow SANS and flow birefringence experiments quantitatively verify the orientation angle predicted by the Giesekus model. However, the discrepancy between the measured alignment factor and the Giesekus prediction is likely due to the specific topology of this long, branched WLM solution.

ACKNOWLEDGMENTS

We thank Unilever and the Humbolt Stiftung (FN) for financial support. Travis Hodgdon completed the Cryo-TEM in Fig. 2. Andrew Klein is acknowledged for assistance in aspects of this research. The authors wish to acknowledge the support of the National Institute of Standards and Technology, U.S. Department of Commerce, in providing the neutron research facilities used in this work. Identification of equipment or materials does not imply recommendation by NIST.

References

Berret, J. F., "Rheology of wormlike micelles: Equilibrium properties and shear banding transition," in *Molecular Gels. Materials with Self-Assembled Fibrillar Network*, edited by R. G. Weiss and P. Terech (Springer, The Netherlands, 2005), pp. 663–716.

Berret, J. F., J. Vermant, and L. Noriez, "Lyotropic surfactant nematics under shear: Neutron scattering in the vorticity plane," in *XIIIth International Congress on Rheology*, Cambridge, UK, 2000, Vol. 3, pp. 273–275.

Britton, M. M., and P. T. Callaghan, "Two-phase shear band structures at uniform stress," Phys. Rev. Lett. **78**(26), 4930–4933 (1997).

Candau, S. J., E. Hirsch, R. Zana, and M. Delsanti, "Rheological properties of semidilute and concentrated aqueous solutions of cetyltrimethylammonium bromide in the presence of potassium bromide," Langmuir **5**(5), 1225–1229 (1989).

Cappelaere, E., J. F. Berret, J. P. Decruppe, R. Cressely, and P. Lindner, "Rheology, birefringence, and small-angle neutron scattering in a charged micellar system: Evidence of a shear-induced phase transition," Phys. Rev. E **56**(2), 1869–1877 (1997).

Caputo, F. E., V. M. Ugaz, W. R. Burghardt, and J.-F. Berret, "Transient 12 plane small-angle x-ray scattering measurements of micellar orientation in aligning and tumbling nematic surfactant solutions," J. Rheol. **46**(4), 927–946 (2002).

Cates, M. E., "Nonlinear viscoelasticity of wormlike micelles (and other reversibly breakable polymers)," J. Phys. Chem. **94**, 371–375 (1990).

Cates, M. E., "Flow behaviour of entangled surfactant micelles," J. Phys.: Condens. Matter **8**, 9167–9176 (1996).

Cates, M. E., "Reptation of living polymers: Dynamics of entangled polymers in the presence of reversible chain-scission reactions," Macromolecules **20**(9), 2289–2296 (1987).

Couillet, I., T. Hughes, G. Maitland, F. Candau, and S. J. Candau, "Growth and scission energy of wormlike micelles formed by a cationic surfactant with long unsaturated tails," Langmuir **20**, 9541–9550 (2004).

Croce, V., T. Cosgrove, G. Maitland, T. Hughes, and G. Karlsson, "Rheology, cryogenic transmission electron spectroscopy, and small-angle neutron scattering of highly viscoelastic wormlike micellar solutions," Langmuir **19**, 8536–8541 (2003).

de Gennes, P. G., *Scaling Concepts in Polymer Physics* (Cornell U.P., Ithaca, NY, 1979).

Decruppe, J. P., S. Lerouge, and J. F. Berret, "Insight in shear banding under transient flow," Phys. Rev. E **63**, 022501 (2001).

Doi, M., and S. F. Edwards, *The Theory of Polymer Dynamics* (Clarendon Press, Oxford, 1986).

Fielding, S. M., and P. D. Olmsted, "Early stage kinetics in a unified model of shear-induced demixing and mechanical shear banding instabilities," Phys. Rev. Lett. **90**, 224501 (2003).

Fielding, S. M., and P. D. Olmsted, "Spatiotemporal oscillations and rheochaos in a simple model of shear banding," Phys. Rev. Lett. **92**(8), 084502 (2004).

Giesekus, H., "A simple constitutive equation for polymer fluids based on the concept of deformation-dependent tensorial mobility," J. Non-Newtonian Fluid Mech. **11**, 69–109 (1982a).

Giesekus, H., "A unified approach to a variety of constitutive models for polymer fluids based on the concept of configuration-dependent molecular mobility," Rheol. Acta **21**, 366–375 (1982b).

Granek, R., and M. E. Cates, "Stress relaxation in living polymers: Results from a poisson renewal model," J. Chem. Phys. **96**(6), 4758–4767 (1992).

Hu, Y. T., and A. Lips, "Kinetics and mechanism of shear banding in entangled micellar solutions," J. Rheol. **49**(5), 1001–1027 (2005).

Hu, Y. T., P. Boltenhagen, and D. J. Pine, "Shear thickening in low-concentration solutions of wormlike micelles. i. direct visualization of transient behavior and phase transitions," J. Rheol. **42**(5), 1185–1208 (1998).

Hu, Y. T., C. Palla, and A. Lips, "Comparison between shear banding and shear thinning in entangled micellar solutions," J. Rheol. **52**, 379–400 (2008).

Humbert, C., and J. P. Decruppe, "Flow birefringence and stress optical law of viscoelastic solutions of cationic surfactants and sodium salicylate," Eur. Phys. J. B **6**, 511–518 (1998).

Kline, S. R., "Reduction and analysis of sans and usans data using igor pro," J. Appl. Crystallogr. **39**(6), 895 (2006).

Kuhn, W., and F. Grun, "Relation between the elastic constant and extension double diffraction of highly elastic substances," Kolloid-Z. **101**, 248–271 (1942).

Liberatore, M. W., F. Nettesheim, N. J. Wagner, and L. Porcar, "Spatially resolved sans in the 1-2 plane: A study of shear-induced phase separating wormlike micelles," Phys. Rev. E **73**, 020504 (2006).

Nettesheim, F., and E. W. Kaler, *Giant Micelles* (CRC, Boca Raton, FL, 2007) Chap. 7, pp. 223–248.

Nettesheim, F., U. Olsson, P. Lindner, and W. Richtering, "Correction method for the asymmetry of the tangential beam in couette (or searle) geometry used in rheo-small-angle neutron scattering," J. Appl. Crystallogr. **37**, 438–444 (2004).

Noirez, L., "Shear induced smectic-a-smetic-c transition in side-chain liquid-crystalline polymers," Phys. Rev. Lett. **84**(10), 2164–2167 (2000).

Noirez, L., and A. Lapp, "Shear flow induced transition from liquid-crystalline to polymer behavior in side-chain liquid crystal polymers," Phys. Rev. Lett. **78**(1), 70–73 (1997).

Olmsted, P. D., "Dynamics and flow-induced phase separation in polymeric fluids," Curr. Opin. Colloid Interface Sci. **4**, 95–100 (1999).

Porte, G., J. F. Berret, and J. L. Harden, "Inhomogeneous flows of complex fluids: Mechanical instability versus non-equilibrium phase transitions," J. Phys. II **7**, 459–472 (1997).

Raghavan, S. R., and E. W. Kaler, "Highly viscoelastic wormlike micellar solutions formed by cationic surfactants with long unsaturated tails," Langmuir **17**, 300–306 (2001).

Raghavan, S. R., H. Edlund, and E. W. Kaler, "Cloud-point phenomena in wormlike micellar systems containing cationic surfactant and salt," Langmuir **18**, 1056–1064 (2002).

Salmon, J.-B., A. Colin, S. Manneville, and F. Molino, "Velocity profiles in shear-banding wormlike micelles," Phys. Rev. Lett. **90**(22), 228303 (2003).

Schubert, B. A., N. J. Wagner, and E. W. Kaler, "The microstructure and rheology of mixed cationic/anionic wormlike micelles," Langmuir **40**, 4079–4089 (2003).

Schubert, B. A., N. J. Wagner, and E. W. Kaler, "The linear viscoelasticity and energetics of charged wormlike micelles," in *XVI International Congress on Rheology*, Seoul Korea (2004a).

Schubert, B. A., N. J. Wagner, E. W. Kaler, and S. R. Raghavan, "Shear-induced phase separation in solutions of wormlike micelles," Langmuir **20**, 3564–3573 (2004b).

Shikata, T., S. J. Dahman, and D. S. Pearson, "Rheo-optical behavior of wormlike micelles," Langmuir **10**, 3470–3476 (1994).

Walker, L. M., and N. J. Wagner, "Sans analysis of the molecular order in poly(g-benzyl l-glutamate)/deuterated dimethylformamide (pblg/d-dmf) under shear and during relaxation," Macromolecules **29**, 2298–2301 (1996).

Yesilata, B., C. Clasen, and G. H. McKinley, "Nonlinear shear and extensional flow dynamics of wormlike surfactant solutions," J. Non-Newtonian Fluid Mech. **133**, 73–90 (2006).